3-D prestack depth migration and velocity model building

Ian F. Jones, Keith Ibbotson, Martin Grimshaw, and Pierre Plasterie, CGG, Feltham, England

Prior to performing a full-volume 3-D prestack depth migration (preSDM), it is necessary to be confident that the velocity-depth model is reliable. The derivation of such a model is addressed here.

However, we first review the limitations of poststack imaging techniques and describe 3-D tomographic inversion, which can be used to derive a good starting model for depth imaging.

Poststack imaging techniques. Conventional time migration does not honor Snell's law of ray bending at interfaces where the velocity changes. As a consequence, the lateral positioning of events is wrong. This error increases in proportion to the dip of the event and the velocity contrasts across geologic horizons. For a salt dome, where dips can exceed 70°, the lateral positioning error of time migration can be in excess of 200 m. Such errors have profound consequences for positioning wells and for estimating reservoir potential.

3-D poststack depth migration (postSDM) can bend rays correctly at interfaces, and it has been employed for some years for iteratively updating layer geometries in velocity-depth model building.

However, this approach can deliver the correct 3-D geometry of an interface only if the preceding interval velocity estimates are accurate. There is also the additional constraint that the subsurface under investigation can be represented by layers.

Given a good velocity-depth model of the subsurface, 3-D postSDM will produce a good "geophysically" positioned image of the earth. This geophysical image may not correspond to the geologic depth, unless such effects as anisotropy are taken into account. If we have been unable to handle the effects of anisotropy during migration, conversion from geophysical depth to geologic depth can be achieved using various postmigration "depthing" processes.

In general, velocities from well logs cannot be used for migration, unless anisotropy is accounted for by the migration algorithm, and the degree (and type) of anisotropy known. Well logs measure the vertical component of the velocity field, which tends to be lower than the horizontal component. It is predominantly the horizontal component which is measured from surface seismic data. And it is this component which should be used to derive the migration velocity field in order to collapse diffraction energy.

Well logs are required, however, to determine vertical compaction gradients and to give the calibration coefficients used for depth conversion of the data after depth migration.

But the main drawback of poststack imaging is the stacking process itself. For complex geologic environments, the moveout observed in CNP gathers is nonhyperbolic; hence the process of NMO/DMO/stack will produce data that are not representative of the desired zero-offset section. Consequently, the subsequent migration will be wrong.

3-D tomographic inversion. The first step in an advanced imaging sequence is to obtain a good starting model of the velocity of the subsurface. We often employ a 3-D tomographic inversion package (TomCad) which uses traveltimes picked from stacked horizons, in conjunction with stacking velocity, and acquisition geometry information to derive a velocity-depth macro-model that is data consistent. A 3-D ray-trace modeler is used to yield an estimate of computed "synthetic" stack times and "synthetic" stacking velocities associated with an initial model which can be produced using conventional normal-ray or image-ray map migration. Residual differences between these "synthetic" data and the observed data are computed for each horizon in the model. A 3-D Marquard-Levenburg inversion scheme (which minimizes these residuals) refines the initial model estimate: The inversion can be performed using either a global or a layer-by-layer scheme. In a global scheme, the residuals for all layers are minimized simultaneously; in a layer-by-layer approach, the residuals are minimized for each layer in turn in a top-down manner.

A number of QC displays are generated. Maps of the residual errors, produced for each horizon, are overlaid by the subsurface "impact points" for that horizon. The impact points show where the 3-D ray bundles from the specified source and receiver locations impinge on a given subsurface horizon. In addition, plots of the shot-receiver azimuth distributions ("spider" diagrams) let the user determine the location of unacceptably binned contributions. The velocity nodes associated with these CMP gathers can be deleted from the input field, or their stacking velocities can be repicked from the CMP gathers, which are also input to the interactive package. Computed traveltimes and stacking velocity trajectories can also be plotted on the CMP gathers to further confirm model validity.

3-D prestack depth migration. This constitutes the ultimate seismic imaging technology because each prestack raypath is individually imaged. Because we avoid stacking in the unmigrated position, the bandwidth of the signal is better preserved and lateral resolution is enhanced. In a Kirchhoff approach, for example, part of the imaging process is the calculation of traveltime trajectories through the velocity-depth model.

Once the traveltimes have been computed for distances along the ray path segments from the shot and the receiver locations to the target element, the Kirchhoff algorithm can be used to affect the prestack imaging. In addition, 3-D image gathers are usually produced which permit evaluation of the velocity field.

Here, we apply the velocity updating technique of Audebert (1996) to iteratively update the interval velocities in a model prior to defining the associated layer geometries.

The CRP image gather scan technique. The core of our approach relies on perturbing the traveltimes so as to span a desired range of velocities.

A unique 3-D preSDM is computed for each, and image gathers are output on a suitable grid. The velocity information can be assessed by analyzing sets of image gathers at each CDP (one gather for each of the perturbation percentages) with an interactive tool, and also by using these ensembles of perturbed gathers to create a 3-D preSDM velocity spectrum, from which the updated velocities can be picked directly. These spectra are created at each CDP location by summing the traces in the CRP gather and computing the envelope of this summation. In addition, the original and updated interval-velocity profiles associated with the original model and the updated picks are displayed.

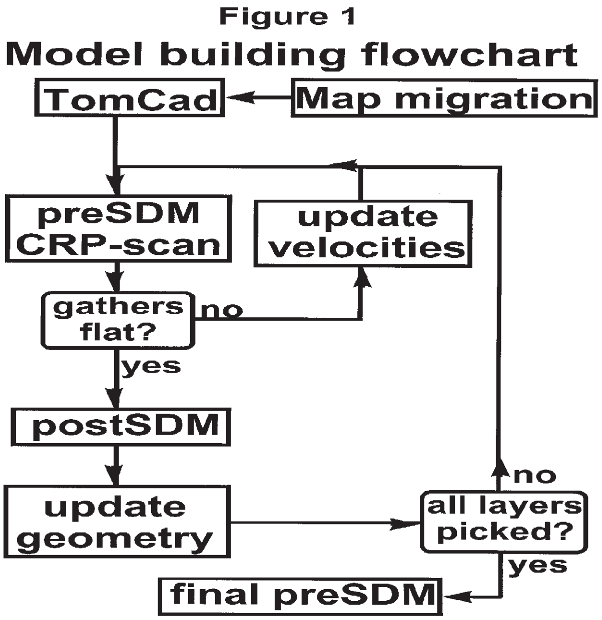

Figure 1. Model building flowchart.

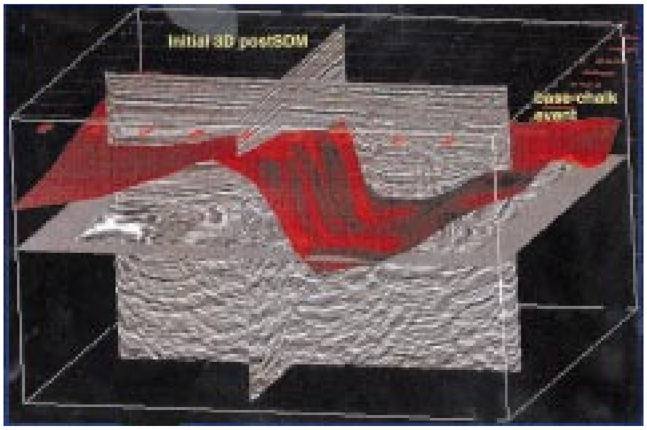

Figure 2. Initial 3-D postSDM.

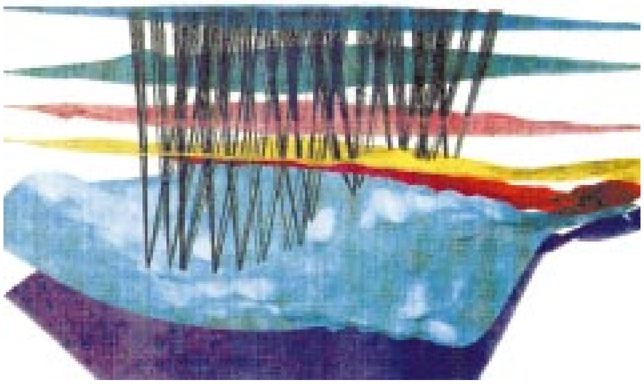

Figure 3. Large-offset rays from CMP gathers.

Although we are primarily attempting to update the velocities for the current layer, we also analyze the residual moveout of deeper events. Even though the deeper horizons may not be completely corrected in the next iteration, a first-order correction should enable the iterative process to converge more rapidly.

Figure 1 is a flow diagram of the most current model-building strategies; in essence this processing flow comprises an inner loop for the interval velocity update (using 3-D preSDM), and an outer loop for the layer geometry update (using postSDM or map migration). Here we use the CRP scan technique in the inner loop.

Our image-gather scan technique is an improvement on the Deregowski loop approach, in that a new 3-D preSDM gather is computed for each value of the perturbation. Hence, for a fixed percentage change, the image in the gather corresponds to a true correction along the normal ray path. Introducing this correction into the velocity-depth model produces accurately corrected imaged data.

North Sea faulted chalk example. We applied this methodology to complex North Sea data. A thick chalk layer, containing three velocity gradient regimes, is faulted with a vertical displacement of about 1.5 km. A deformed salt layer, a further 1 km below the chalk, poses additional problems. The zone of interest lies below the overhanging footwall of the fault.

In the initial model, the fault plane was nowhere overhanging, as the 3-D postSDM images were insufficiently clear to permit meaningful interpretation of the overhang. Figure 2 shows a 3-D postSDM result superimposed on the base-chalk event. Here the fault is represented by the steep element of the base chalk and is not overhanging. Explicit representations of the over-

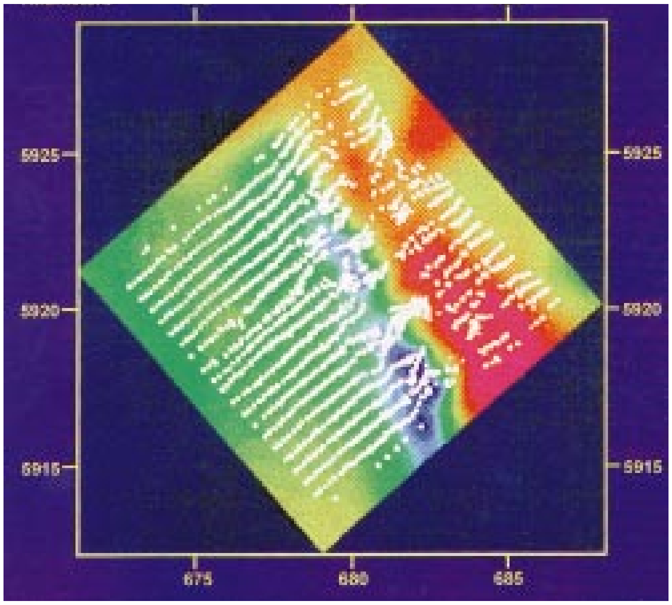

Figure 4. Ray tracing on initial model; impact on base chalk.

CRP image gather scan and spectrum

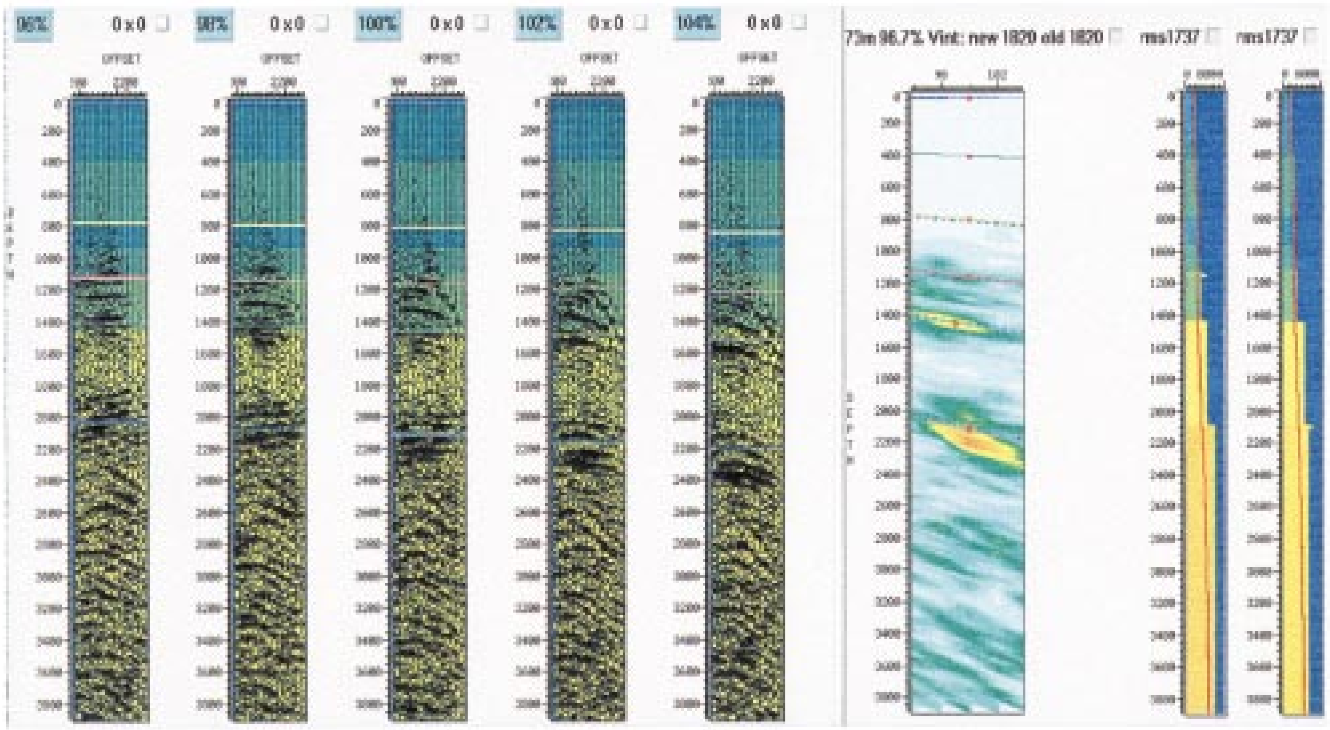

Original Z **Original Vi**

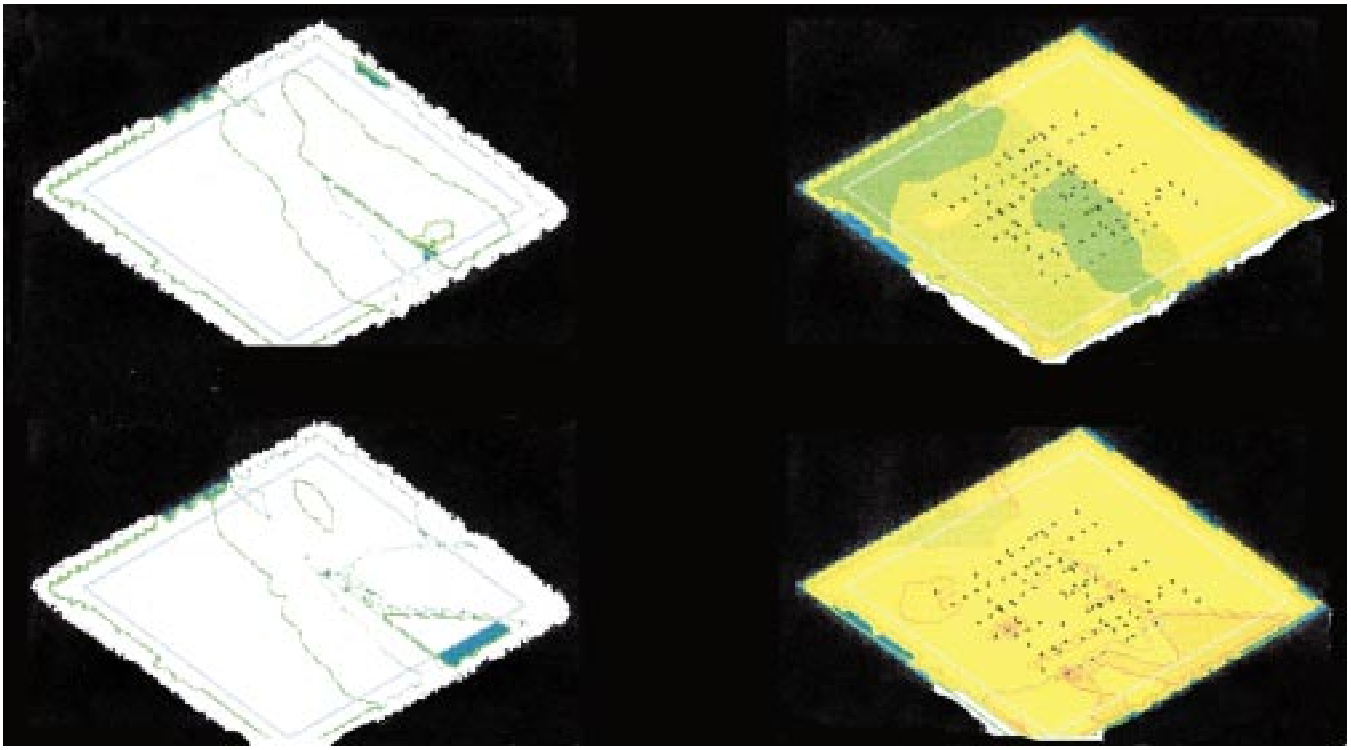

Updated Z **Updated Vi**

Figure 5. Interactive pre-SDM velocity update.

a)

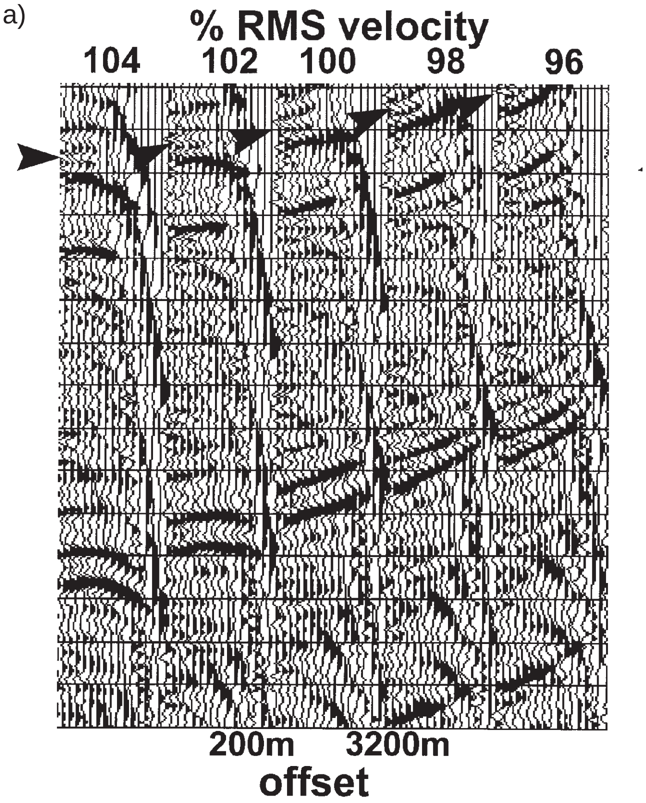

b)

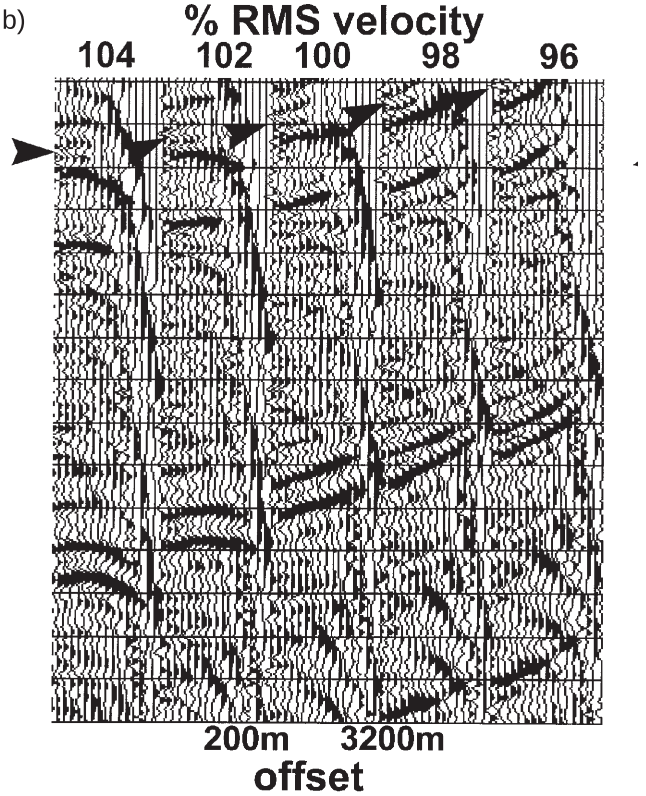

Figure 6. 3-D preSDM image gather scan. (a) Initial model and (b) Second model. Numbers at the top are the percentage of RMS velocity.

hanging fault were incorporated in later models.

For the shallower overburden, down to and including the top-chalk horizon, analysis of the image gathers was unable to assist in defining the velocity-depth model, as the fold of coverage in the gathers was too low, and

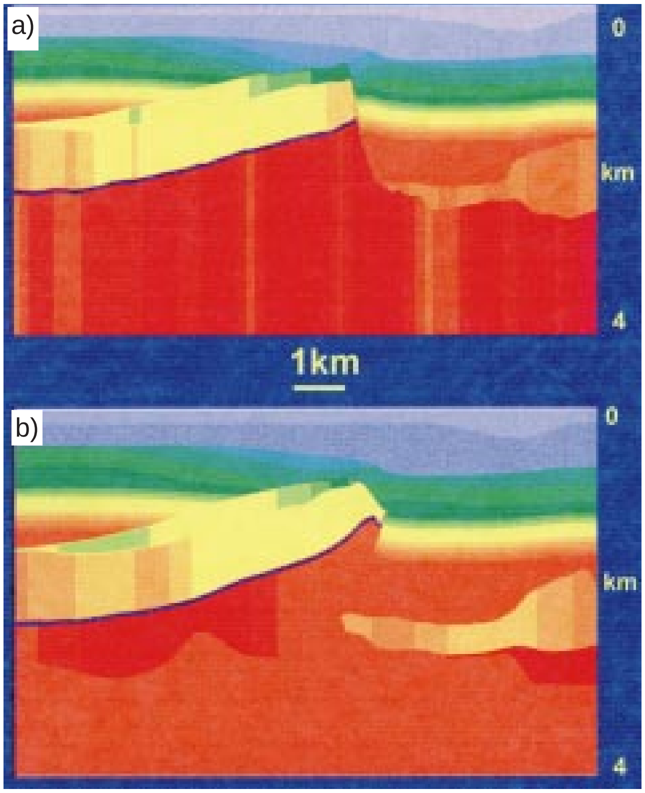

Figure 7. (a) Initial model. (b) Final model.

insufficient velocity discrimination was afforded. 3-D tomographic inversion was used in an attempt to estimate the velocity field for this low-fold seismic overburden.

Model building. The first step was to obtain interval velocities based on Dix inversion of stacking velocities derived using a machine-guided velocity picking routine. The next step consisted of building an initial depth model using map migration of zero-offset traveltimes incorporating vertical velocity gradients from well logs. This was followed by 3-D tomographic inversion of zero-offset traveltime and stacking velocities to derive an updated model. Figure 3 shows the 3-D ray bundles associated with the initial model for the base-chalk event. Figure 4 shows the impact points of these ray bundles projected onto a map of the base-chalk horizon.

From the tomographic inversion, we obtained the near-surface velocity field. However, we concluded the results were less reliable than the image gather analysis for the deeper, more complex horizons.

The first computation of the traveltimes was based on the initial model and used to drive the preSDM on a coarse grid of lines to produce migrated images along each line and a scan of image gathers every 500 m along the lines (using 5% perturbations of the traveltime file to create the scan images).

Events above and including the top chalk could not be updated, as the low fold did not permit velocity discrimination. However, for the base chalk, Rot Halite, Zechstein, and Rotleigendes layers, model update was feasible with this technique.

Figure 5 is a screen capture of the CRP-scan tool for picking the velocity model updates from image-gather scans. The percentage perturbations can be converted to preSDM velocity analysis panels, analogous to focusing analysis panels (upper right) as well as being viewed directly as image gathers, with the associated perturbed velocity models superimposed (upper left). The lower part of the figure shows the initial interface map and interval velocity map, as well as the updated versions of these maps (as picked interactively by the user). Superimposed on the maps are the spatial locations of the image gathers.

We chose five perturbations of the traveltimes (96%, 98%, 100%, 102%, 104%). If a gather is flat for a given percentage, then updating the entire model by this amount will guarantee that a new migration produced with updated traveltimes will produce a correct preSDM image, as the perturbation is accumulated along normal ray paths and not simply in a vertical sense. As mentioned above, our method assumes that the perturbation to the model varies slowly in a lateral sense.

In the example shown here, the perturbation was to the entire model, and therefore concerns the RMS velocity down to a layer. Thus, for the iteration designed to update a given horizon, the correction for this perturbed horizon would be “exact” if we were to accept a globally constant percentage correction. A first-order approximation permits conversion to interval velocity corrections for any subsequent horizons should a different percentage correction be required. However, given that we do not in general want to perturb the entire model (as the overburden may have been corrected already) we must back out the effect of the overall correction from the overburden before defining the updated interval velocity for the current layer. This can be achieved vertically or in 3-D by inverting back along the normal ray paths.

Scans on image gathers for the different traveltime perturbations are produced for each iteration for all nodes in the coarse velocity grid. For example, we show results derived from the first iteration where a spatially and vertically variant correction field was picked in order to flatten the base-chalk event, and approximately flatten subsequent events. Following this (and each subsequent) iteration of velocity update, we perform a 3-D postSDM to determine the layer geometry for this layer by picking the horizon imaged directly in depth. Because we also attempt to correct the deeper layers (to a first-order approximation), we also need to adjust the depths (horizon geometries) of these layers in accordance with their updated velocities. We achieve this with map migration.

After incorporation of the velocity update and layer geometry picking into the model, recomputing the traveltimes and rerunning the 3-D preSDM, we found that the base-chalk event was flattened, and subsequent events were better imaged.

Figure 6a shows the image-gather scan for a single CDP location for iteration 1 of the 3-D preSDM. The arrow is the base-chalk reflector which exhibits a strong vertical velocity gradient in the model (Figure 7). The base-chalk and Rot Halite layers called for a 4% increase in velocity over the southern half of the survey, which fell to a 2% increase at the northernmost part. The Zechstein called for a reduction relative to the increase in velocity of the evolving layers. After performing analyses of such image gather scans for all control nodes on the 500 × 600 m grid, the velocity field was updated, the geometries repicked from a 3-D postSDM, and the image gathers recomputed.

After the second iteration of 3-D preSDM (Figure 6b),

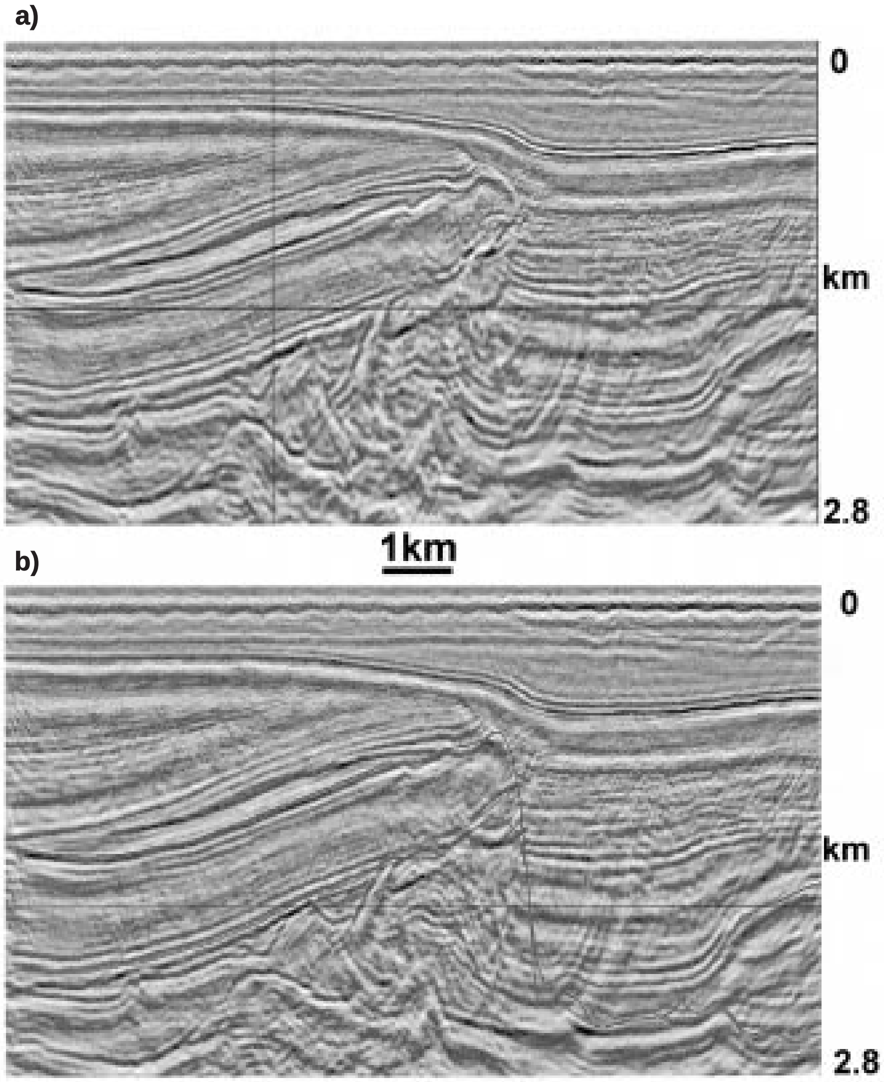

Figure 8. (a) 3-D postSDM initial model. (b) 3-D postSDM third model.

the image gathers now show well-corrected events down to the Rot Halite (1.5 km) and need updating for the Zechstein and below. We now see that the base chalk event has been correctly imaged at this location. We also attempted to correct other events during the first iteration; consequently most of the subsequent reflections are reasonably well corrected by the second iteration.

Figure 7a is the velocity-depth profile from the initial model and Figure 8a the corresponding 3-D postSDM result. In addition, the postSDM produced after the third iteration (Figure 8b) clearly indicates the position of the overhang on the fault, as well as improving the imaging of the Rotleigendes (about 2.5 km on the right of the figure). The near-vertical superimposed marker in Figure 8b is the position of the fault as picked on Figure 8a. We now see that the near-horizontal events below 2 km extend farther to the left of the initial fault interpretation.

During the model-building process, five iterations of 3-D preSDM and 11 iterations of 3-D postSDM were employed. Each iteration progressly improved horizon consistency under the fault overhang. By the end of the model building, many subtle changes were made to the model, including introduction of an overhang on the fault (Figure 7b).

The following figures demonstrate the differences between the quality of imaging discernible between prestack and poststack depth migration. Using the same final velocity model, we see in Figures 9a and Figure 9b the 3-D postSDM and 3-D preSDM results for an in-line. A narrow wrench fault graben appears smeared in the postSDM result but well imaged in the preSDM. This gives a clear indication that stacking has damaged the data which defines the fault edges.

For the cross-line direction, the images of the block-faulted lower portion of the images (between 2.4 and 2.7 km) are better focused in the 3-D preSDM (Figure 10b) than in the 3-D postSDM (Figure 10a). The arrow indicates the location of intersecting lines.

Convergence. During model updating, we generated percentage correction grids associated with those layers modified during each iteration. An investigation of how these required updates evolved gave some insight into the convergence of the velocity updating process.

Figure 11 shows the image-gather scans for the Zechstein during the first, second, and third model updates. An overlying event was being updated, but it can be seen that, during the successive iterations, the model is converging for deeper layers.

An alternative investigation of convergence could have been to review the residual error associated with the modeled and observed data (stack times and stacking velocities) associated with the various models. However, we found from the residual error maps associated with the starting and penultimate models that there was no discernible difference in model "accuracy" from this "poststack" perspective. This indicates that the level of detail introduced into the model during preSDM update using image gathers lies in the "null space" of the tomographic inversion procedure. That is to say, the nature of the changes introduced to the initial model in order to eventually create the latter model are such that performing finite offset ray tracing through the model and then fitting a hyperbola to the results cannot meaningfully discriminate between these two models on the basis of overall error.

This points to the limitations of a "poststack" inversion approach: The same hyperbolic fit matches the finite-offset data computed for the initial and final models equally well. In other words, the differences between these models which do indeed result in improved pre- and poststack images must lie in the nonhyperbolicity of the diffraction response of the velocity-depth model.

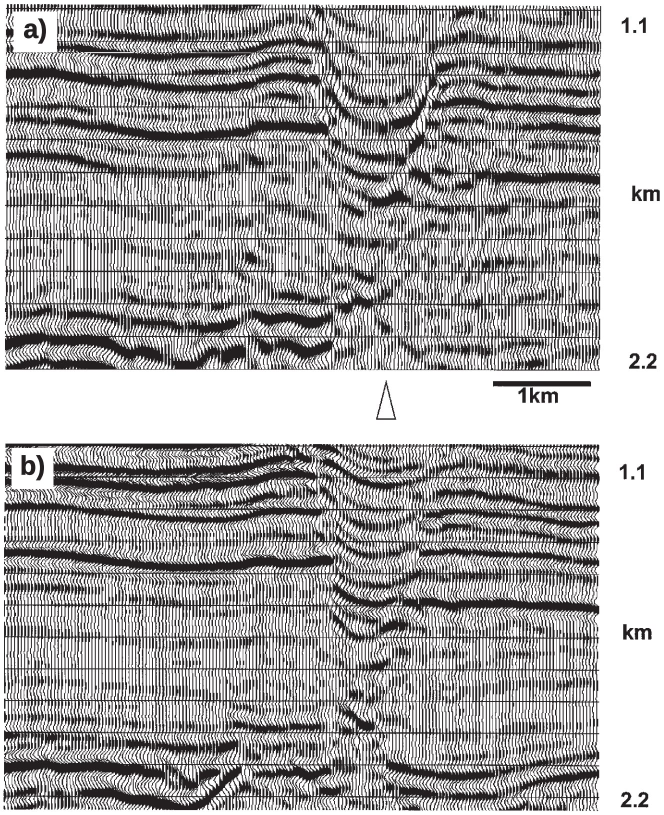

Figure 9. (a) 3-D postSDM with final model. (b) 3-D preSDM with final model.

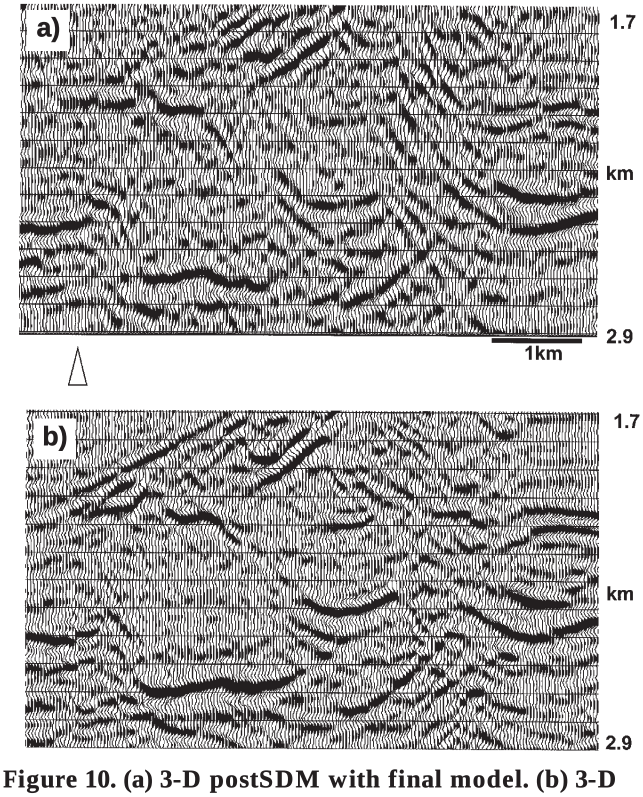

Figure 10. (a) 3-D postSDM with final model. (b) 3-D preSDM with final model.

Conclusions from this example. Throughout the iterations of model building, the associated postSDM images showed a progressive improvement in the resolution of deeper events. Image gathers for each iteration also showed a general "flattening" of events and the final iteration produced the best image gathers.

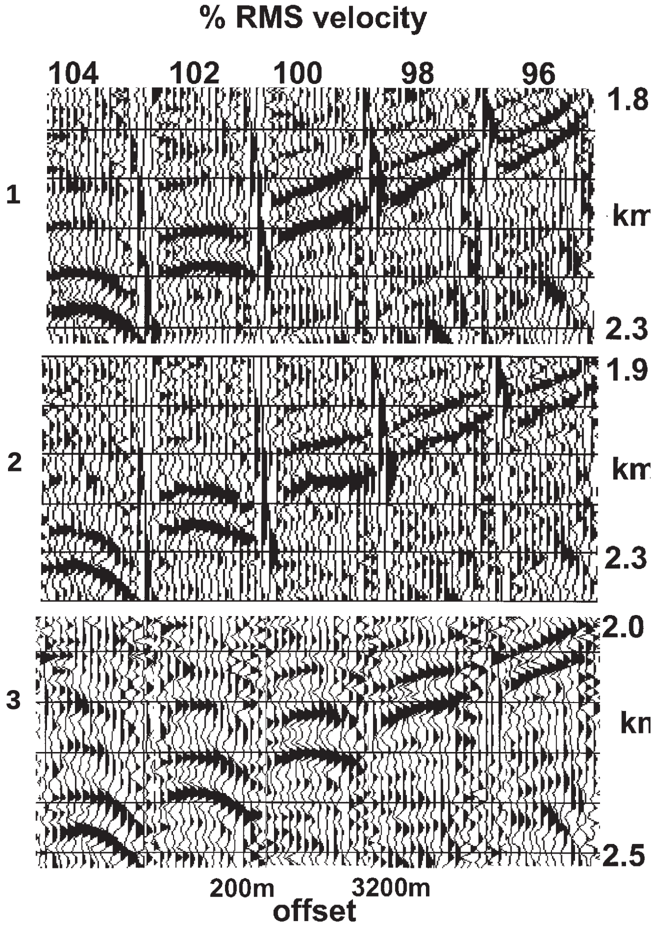

Figure 11. 3-D preSDM image gather scan. Progressive results for the Zechstein.

For this type of structure, where the geology is predominantly cylindrical, acquiring data in the strike direction (as was the case here) will give rise to the best possible stacked section, and thereby facilitate the production of a good postSDM image. However, because the raypaths in this acquisition avoid complexities in the dip direction, a preSDM result obtained with these data will be suboptimal. Further, for structures such as this, or for tabular salt bodies, the zero-offset ray-path can take different routes on the downgoing and upgoing paths near the edge of the body. This will generally violate the assumptions we made in preparing the traveltimes for preSDM.

Conversely, acquiring data in the dip direction will give rise to an inferior stack and postSDM result but will be better suited to forming an adequate preSDM image. This raises the question of whether strike acquisition is appropriate when the final products are to be prestack migrated. Unfortunately, acquisition practitioners or economics usually decide the shooting direction.

Residual moveout correction of final migrated CRP gathers. In an approach analogous to residual NMO correction of time-processed data, we introduce here a technique for automatically estimating and applying a residual depth error correction to the image gathers prior to summation to form the final image. The approach is based on the approach of Doicin et al. (1995), wherein

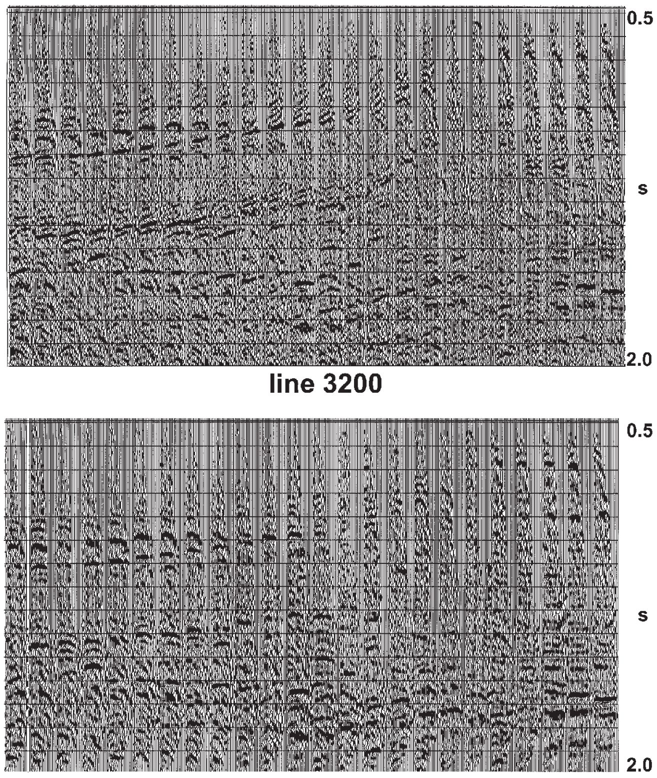

Figure 12. 3-D preSDM image gathers which (a) result from initial model and (b) result after residual correction of all CRPs.

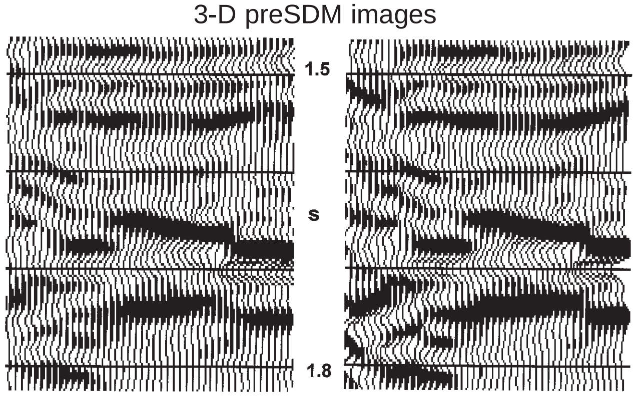

Figure 13. 3-D preSDM images before RMO (left) and after RMO (right).

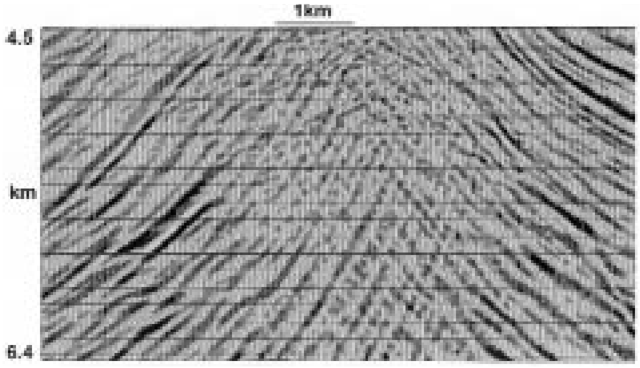

Figure 14. 3-D postSDM image resulting from final salt-dome model.

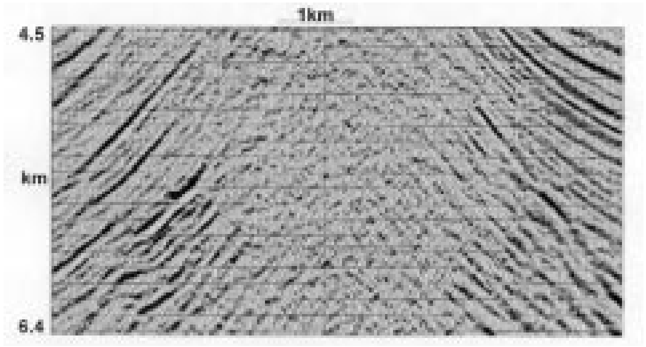

Figure 15. 3-D preSDM image resulting from final salt-dome model.

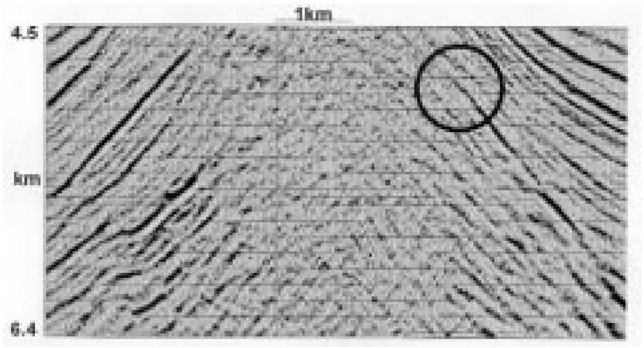

Figure 16. 3-D preSDM image resulting from RMO corrected CRP gathers.

approximately flattened gathers are perturbed with residual moveout and then summed using a suite of trial perturbations to form the basis of a coherency scan: The residual moveout associated with the maximum local stack power is adopted to perform the residual NMO correction. This operation is performed for all CDP locations and all time samples. Prior to acceptance of the updated moveout correction, several statistical tests are performed to reject multiple events and events which exhibit poor spatial continuity.

A variation of this technique (Jones et al. 1997) was applied to the image gathers from the initial iteration of preSDM on the chalk example. Figure 12a and Figure 12b show the CRP gathers before and after this procedure (every eighth CRP gather is displayed, but all were processed). Although the model building and imaging are not completed at this stage, a stack of the image gathers with the residual correction shows a significant improvement over the stack of the uncorrected CRP gathers (Figure 13).

North Sea salt diapir example. The second example is a typical North Sea central graben salt dome. The velocity-depth model was constructed using iterative application of TomCad in conjunction with postSDM layer stripping.

Upon completion of the 3-D postSDM model, a target-oriented 3-D preSDM was performed. The image gathers were subjected to the automatic residual moveout correction described above. Figure 14 is an in-line section from the 3-D postSDM showing the deeper flanks of the diapir. Figure 15 is the corresponding 3-D preSDM image. The velocity-depth model is the same in both cases. The lower-frequency appearance of the postSDM is due to the smearing of the stacking process. After application of the residual moveout correction on all CRP image gathers of the 3-D preSDM output and subsequent stacking of these corrected CRP image gathers, we obtain Figure 16. Overall, we have better continuity of events; for example, the steeply dipping segment of the reflection between 4.8 and 5.0 km (indicated by the circle) extends vertically a further 200 m in the residual-moveout corrected image.

Our observations to date with this new residual error correction technique indicate it provides additional benefits in improving the imaging for horizons not explicitly included and described in the velocity-depth model.

Naturally, this RMO procedure does not replace the model-building effort; its purpose is to allow us to obtain the best possible image for a given final model.

Conclusions. Prestack depth imaging can yield significant improvement over conventional poststack depth imaging, especially when high-resolution, high-fidelity imaging is required. However, the velocity-depth model of the subsurface must be accurately determined.

We have demonstrated a new technique which moves us closer to this goal. In addition, the automated residual moveout correction technique, as applied to CRP depth image gathers, gives a final fine-tuning of the image.

Suggestions for further reading. "Iso-x-gathers as a combination of common reflection gathers and velocity scans" by F. Audebert (1996 *EAGE Annual Meeting*). "Common-offset migrations and velocity analysis" by S. Deregowski (*First Break*, 1990). "Continuous 3-D preSDM velocity analysis" by Jones et al. (1997 SEG *Expanded Abstracts*). "Machine guided velocity interpretation" by D. Doicin et al. (1995 *EAGE Annual Meeting*). LE

Acknowledgments: Our thanks to Shell UK, Esso UK, and Elf Norge for their kind permission to use their data. Thanks also to our CGG colleagues for their support in preparing the material, especially to the members of the Paris research group: Jean-Paul Diet, Laurence Boissy, Antonio Pica, Francois Audebert, Patrice Guillaume, and Jean-Yves Blanc. This work was supported in part by the European Commission Thermie initiative project OG/00188/94/FR.

Corresponding author: Ian Jones, email ianjones01@aol.com or ifjones@cgg.com